entropy

MDPI

Article

Numerical Simulation of Williamson Combined Natural and Forced Convective Fluid Flow between Parallel Vertical Walls with Slip Effects and Radiative Heat Transfer in a Porous Medium

Mohammad Yaghoub Abdollahzadeh Jamalabadi [1,*], Payam Hooshmand [2], Navid Bagheri [3], HamidReza KhakRah [4] and Majid Dousti [5]

1 Department of Mechanical, Robotics and Energy Engineering, Dongguk University, Seoul 04620, Korea
2 Department of Mechanical Engineering, Sanandaj Branch, Islamic Azad University, Sanandaj 6616935391, Iran; payam.hooshmand@yahoo.com
3 Department of Energy Engineering, Graduate School of the Environment and Energy, Science and Research Branch, Islamic Azad University, Tehran 1477893855, Iran; navidbagheri777@yahoo.com
4 Department of Mechanical Engineering, College of Engineering, Shiraz Branch, Islamic Azad University, Shiraz 71987-74731, Iran; hrkhakrah@yahoo.com
5 Faculty of Engineering, Zanjan University, Zanjan 38791-45371, Iran; dousti.mj@znu.ac.ir
* Correspondence: abdollahzadeh@dongguk.edu or muhammad_yaghoob@yahoo.com; Tel.: +82-22-260-3073

Academic Editor: Milivoje M. Kostic
Received: 29 February 2016; Accepted: 8 April 2016; Published: 18 April 2016

Abstract: Numerical study of the slip effects and radiative heat transfer on a steady state fully developed Williamson flow of an incompressible Newtonian fluid; between parallel vertical walls of a microchannel with isothermal walls in a porous medium is performed. The slip effects are considered at both boundary conditions. Radiative highly absorbing medium is modeled by the Rosseland approximation. The non-dimensional governing Navier–Stokes and energy coupled partial differential equations formed a boundary problem are solved numerically using the fourth order Runge–Kutta algorithm by means of a shooting method. Numerical outcomes for the skin friction coefficient, the rate of heat transfer represented by the local Nusselt number were presented even as the velocity and temperature profiles illustrated graphically and analyzed. The effects of the temperature number, Grashof number, thermal radiation parameter, Reynolds number, velocity slip length, Darcy number, and temperature jump, on the flow field and temperature field and their effects on the boundaries are presented and discussed.

Keywords: radiative heat transfer; slip effects; natural convection; forced convection; microchannel; porous medium

1. Introduction

Combined natural (free) and forced convection in channels occurs in many applications [1] and geometries such flow between parallel vertical walls [2], including flow reversal [3], inclined parallel plates [4], and vertical channels [5], *etc.* Thermal radiative emission from a hot surface to a cold surface plays an important role in many uses, including energy conversion [6], with radiation effects and viscous heating in a channel partially filled by a porous material [7], viscous heating in a porous channel [8], microchannels [9], heat exchangers with vertical hexagonal rod bundle geometries [10], buoyancy-driven vortical flow [11], biofidelity corridors [12], fluid flow control [13,14], in various boundary conditions [15], and pressure dependent viscosity flows [16]. Furthermore mixed convection viscoelastic slip flow through a porous medium in a vertical porous channel with thermal radiation flow [17] is found in industrial processes and has acquired substantial importance due to its wideranging applications in fluid flow control [18], propulsion [19,20], and viscous gravity currents inside confining channels and fractures [21,22].

Velocity and thermal slip affects high performance magnetic bearings that are subjected to higher thermal loads and many other research fields [23–26], EHD (electrohydrodynamics) mixers [27], microfluidics and nanofluidics [28–32], and pseudoplastic material hydrodynamics [33–38]. The flow slip at boundary conditions is seen in rare gas flow [28] as well as incompressible flow [29]. In addition, thermal jump conditions are seen in many experiments [30]. Ulmanella and Ho [29] experimentally detected the speed of fluids at several microchannel walls, as a function of shear rate, type of fluid, and wall surface properties. Bocquet and Barrat [30] explained the probability of temperature slip simultaneously with velocity discontinuity at boundary conditions. They presented the amount of velocity slip and the value of temperature jump by bringing together the velocity slip length and temperature slip length, respectively. The slip relations should be applied at the fluid solid boundaries in microchannels in other textbooks [31].

Recently Jha *et al.* [32] presented an exact solution of steady fully developed natural convection flow of a viscous, incompressible, electrically conducting fluid in a vertical annular microchannel with the effect of porous resistance in the presence of velocity slip and temperature jump at the annular microchannel surfaces [32]. They expressed their solution in terms of radius ratio, Darcy number, rarefaction parameter, and fluid–wall interaction parameter effect on the flow. They found that an increase in Darcy number leads to a decrease in the fluid velocity, volume flow rate and skin friction, but they have not studied the effects of parameters on Nusselt number and their geometry is cylindrical.

Of the various kinds of fluids the Williamson fluid is studied in this paper. The Williamson fluid was first introduced by Williamson in 1929 [33]. This kind of fluid model was first is used to model pseudoplastics which do not exhibit a real yield value and cannot be modeled as plastics nor Newtonian fluids. Gravity currents such as drainage processes may occur in a variety of natural and industrial activities, including the geological storage of carbon dioxide. This kind of non-Newtonian fluid behavior is observed in gravity currents propagating in confining boundaries [34] in volcanos and geothermal applications [35]. King and Woods [36] presented a dipole solution for viscous gravity currents. Longo *et al.* illustrated the dipole solution for power-law gravity currents in porous formations [37]. Buoyancy-driven fluid drainage from a porous medium for V-shaped Hele-Shaw cells where the fluid drains from an edge is discussed in another reference. It flows between walls with a limited gap (with respect to the main length scales) mimicking flows in porous media (Hele-Shaw cell analogy) [38].

Considering all the above, the aim of the current study was the synthesis of the radiative hydrodynamics of a highly absorbing incompressible fluid in a straight up microchannel filled with a saturated porous material. Different wall temperatures are applied on the walls of the channels and the fluid is an optically thick medium. A parameter study on temperature profile, velocity profile, Nusselt number, and friction coefficient is investigated analytically.

2. Materials and Methods

A two-dimensional, steady state, incompressible and electrically conducting fluid flow with heat transfer by convection between two vertical plates in the presence of radiation in a simple configuration as shown in Figure 1. A stream of cold fluid at temperature T_L moving over the left surface of the plate with a slip velocity formed a fully developed laminar flow while the right surface of the plate is heated by convection from a hot fluid at temperature T_R .The two parallel planar walls are located at $y = -\mathrm{L}$ and $y = +\mathrm{L}$, with the gap of 2 L. We shall assume that the velocity and the pressure field are of the form:

$$\vec{V} = (u(y), 0, 0) \qquad \mathrm{p} = p(\mathrm{x}) \tag{1}$$

The equation which governs the buoyancy-driven flow of an incompressible fluid through a porous medium in the x-direction is:

$$\rho \left(u \frac{\partial u}{\partial x} + v \frac{\partial u}{\partial y} \right) = -\frac{\partial p}{\partial x} + \frac{\partial \tau}{\partial y} - \rho_0 g \beta \left(T - T_{ref} \right) + uK \tag{2}$$

Since in other directions there is no fluid flow, the corresponding equations are not required here. The Navier–Stokes equation for steady state fully developed velocity ($\partial u/\partial x = 0$; $\partial^2 u/\partial x^2 = 0$) for the case for which $\mu_\infty = 0$, $\mu_0 = \mu$ and $\Gamma\gamma' < 1$ (the component of extra stress tensor is $\tau = \mu\gamma' \left(1 - \Gamma\gamma'\right)^{-1} = \mu\gamma' \left(\Gamma\gamma' + 1\right)$) [16] can be written as is simplified as:

$$\frac{d^2 u}{dy^2} = \frac{\frac{dp}{dx} + uK - \rho_0 g \beta \left(T - T_{ref} \right)}{\mu \left(1 + 2\Gamma \frac{du}{dy} \right)} \tag{3}$$

where u is the fluid velocity in vertical direction, ρ_0 is the fluid density at reference temperature ($T_{ref} = (T_L + T_R)/2$), μ is the dynamic viscosity, β is the thermal expansion coefficient, and σ_c is the electrical conductivity. As well, the temperature equation for optically thick fluid is [18]:

$$\frac{\partial^2 T}{\partial y^2} = -\frac{4\sigma}{3k\chi} \frac{\partial^2 T^4}{\partial y^2} \tag{4}$$

where T is the medium temperature, k is the thermal conductivity, σ is the Stefan–Boltzmann constant and χ is the mean absorption coefficient of the medium. The boundary conditions of Equation (1) at the system boundaries are:

$$u\left(y = L\right) = l_v \left(\frac{du}{dy} \right)_{y=L} \tag{5}$$

$$u\left(y = -L\right) = l_v \left(\frac{du}{dy} \right)_{y=-L} \tag{6}$$

where l_v is the velocity slip length and for the temperature are:

$$T\left(y = L\right) = T_R + l_T \left(\frac{dT}{dy} + \frac{4\sigma}{3k\chi} \frac{\partial T^4}{\partial y} \right)_{y=L} \tag{7}$$

$$T\left(y = -L\right) = T_R + l_T \left(\frac{dT}{dy} + \frac{4\sigma}{3k\chi} \frac{\partial T^4}{\partial y} \right)_{y=-L} \tag{8}$$

where l_T is the temperature jump length. The above equations are non-dimensionalized by the following parameters for length:

$$X = \frac{x}{L} \tag{9}$$

$$Y = \frac{y}{L} \tag{10}$$

for velocity:

$$U\left(Y\right) = \frac{u(y)}{u_m} \tag{11}$$

for temperature:

$$\theta\left(Y\right) = \frac{2T - T_L - T_R}{T_R - T_L} \tag{12}$$

for pressure:

$$P = \frac{pL}{\mu u_m} \tag{13}$$

and the non-dimensional well-known numbers as Grashof number:

$$Gr = \frac{g\beta\,(T_R - T_L)\,L^3}{2\nu^2} \tag{14}$$

Reynolds number:

$$\mathrm{Re} = \frac{u_m L}{\nu} \tag{15}$$

the radiation parameter:

$$R_d = \frac{\sigma\,(T_R - T_L)^3}{6k\chi} \tag{16}$$

temperature parameters:

$$\theta_R = \frac{T_R + T_L}{T_R - T_L} \tag{17}$$

Darcy number:

$$Da = \frac{L^2}{K} \tag{18}$$

Weissenberg dimensionless number:

$$We = \frac{\Gamma u_m}{L} \tag{19}$$

Which is used for comparison of the evolution of the viscous energy released to the elastic energy stored in the viscoelastic fluid flows, defined as the relation of stress relaxation time of the fluid (Γ) and the fluid flow time (*u/L*). Physical interpretation of the Weissenberg number is the degree of anisotropy or orientation generated by the deformation, and it is appropriate to describe flows with a constant stretch history, such as simple shear.

Velocity slip parameter:

$$\lambda_v = \frac{l_v}{L} \tag{20}$$

$$\lambda_T = \frac{l_T}{L} \tag{21}$$

Finally the non-dimensional governing equations can be reformulated as:

$$\frac{d^2U}{dY^2} = \frac{DaU - \frac{Gr\theta}{\mathrm{Re}} + \frac{dP}{dX}}{1 + We\frac{dU}{dY}} \tag{22}$$

$$\frac{d^2}{dY^2}\left[\theta + R_d(\theta + \theta_R)^4\right] = 0 \tag{23}$$

$$U\,(Y = 1) = \lambda_v \left(\frac{dU}{dY}\right)_{Y=1} \tag{24}$$

$$U\,(Y = -1) = \lambda_v \left(\frac{dU}{dY}\right)_{Y=-1} \tag{25}$$

$$\theta\,(Y = 1) = 1 + \lambda_T \frac{d}{dY}\left[\theta + R_d(\theta + \theta_R)^4\right]_{Y=1} \tag{26}$$

$$\theta\,(Y = -1) = -1 + \lambda_T \frac{d}{dY}\left[\theta + R_d(\theta + \theta_R)^4\right]_{Y=-1} \tag{27}$$

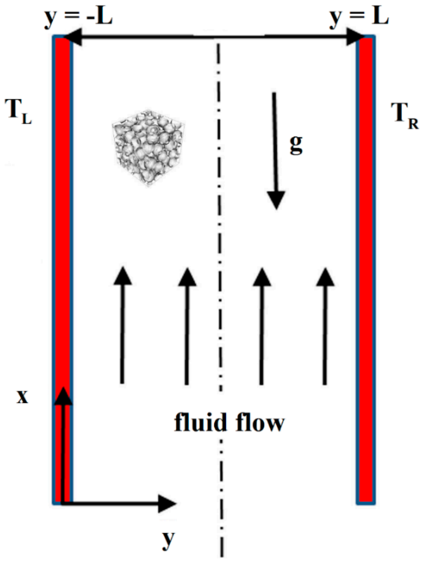

Figure 1. Schematic illustration of a vertical channel containing fully-developed mixed convection fluid flow.

3. Results and Discussion

Research has been carried out into steady state laminar combined free and forced convection fluid flow in a upright channel occupied by a highly absorbing fluid, which are important factors in various industrial applications. For the purpose of obtaining a strong visualization of the physical problem, widespread estimations have been performed to acquire the velocity and thermal field as a function of physical parameters such as combined convection parameter and Darcy number temperature-based parameters such as thermal radiation parameter, thermal parameter, and temperature slip, and a flow parameter, the velocity slip, are exposed comprehensively in Figures 2–7. The non-dimensional governing Equations (19)–(24) are solved numerically using Runge–Kutta–Fehlberg method with shooting technique. The set of simultaneous first order differential equations of equivalent initial-value problem ($Z' = f(Z,Y)$) are constructed by the vector $Z = [U; U'; \theta; \theta']$ and the first guess of the initial value are assumed as $Z(Y = -1) = [0; 0; -1; 0]$.

To benchmark the current numerical method, the comparison of the numerical solution and analytical solution is illustrated in Figure 1. As the analytical solution of the problem for $R_d = 0.0$, $\Gamma = 0$, and $\lambda_T = 0.0$ is:

$$\begin{aligned} U = {} & \frac{Gr}{\mathrm{Re}.Da}Y - \frac{P_X}{Da} \\ & + \frac{e^{-\sqrt{Da}.Y}\left(2\frac{Gr}{Re}cosh\sqrt{Da} + 2P_X sinh\sqrt{Da} + 2\frac{Gr}{Re}l_v sinh\sqrt{Da}\right)}{2Da.sinh(2\sqrt{Da})(\sqrt{Da}l_v + 1)} \\ & - \frac{e^{\sqrt{Da}.Y}\left(2P_X sinh\sqrt{Da} - 2\frac{Gr}{Re}cosh\sqrt{Da} + 2\frac{Gr}{Re}l_v sinh\sqrt{Da}\right)}{2Da.sinh(2\sqrt{Da})(\sqrt{Da}l_v - 1)} \end{aligned} \tag{28}$$

where pressure drop is calculated from:

$$\begin{aligned} & \left(\frac{2}{e^{2\sqrt{Da}}+1} - 1\right)\left(P_X + \frac{Gr}{Re}l_v\right) + \sqrt{Da}P_X = \\ & Da^{3/2}{l_v}^2 P_X - \frac{Gr}{Re}\sqrt{Da}l_v + Da^{3/2}(Da{l_v}^2 - 1) \end{aligned} \tag{29}$$

The numerical results of current work for velocity slip length of 0.01, $Da = 0.01$, and $Gr/Re = 50$ are in good agreement with the analytical solution. As shown in Figure 2 the shooting method can capture the precise results with 15 points. Figure 2 presents the consequence of the change of thermal radiation parameter on the numerous feature of temperature and velocity field of the microchannel in the constant value of the Grashof to Reynolds ratio ($Gr/Re = 100$), and $\theta_R = 10$, $\lambda_v = 0.01$, $We = 0.001$, $\lambda_T = 0.01$, $Da = 0.1$. On behalf of the special case of no absorption of the thermal radiation in the fluid, the temperature has a linear profile as shown in Figure 3a. By increasing of thermal radiation number ranging 10^{-4} to 10^{-2} the dimensionless temperature is amplified, particularly close to the left partition. Figure 3b displays a curvy form for the velocity outline. By growth of the amount of thermal radiation, the dimensionless velocity profile alternates from sine shape to parabola shape and its maximum decrease. The maximum value occurs at the middle of parabola profile approaches the Poiseuille profile maximum (*i.e.*, 1.5) by increase of R_d. The effect of thermal radiation on the friction factor at walls and pressure gradient is illustrated in Figure 3c. By increasing R_d, the friction factor at the walls (the left and right friction coefficients) decrease smoothly while the pressure gradient (the profile with the middle legend), increases dramatically. As well the friction factor for the same Reynolds number is greater at the right wall for low R_d and the reverse phenomena is seen for high R_d. Both skin-friction values continue to reduce further with the increase of R_d although the rate of reduction declines. The Nusselt number profiles are plotted *versus* R_d at the walls in Figure 3d. The augmentation is more sensitive in the right wall. The change in the heat amount at the left and the right surface is the same as the absorbed heat in the system.

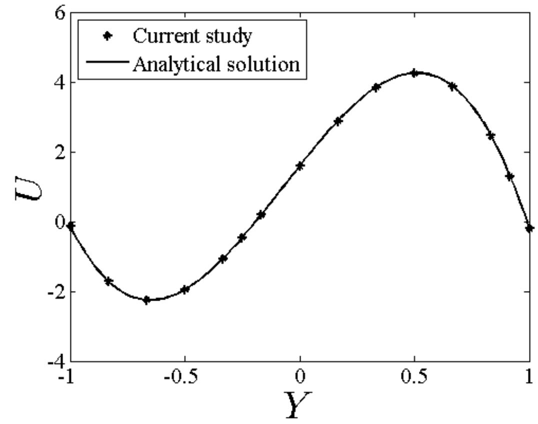

Figure 2. Comparison of numerical solution and analytical method.

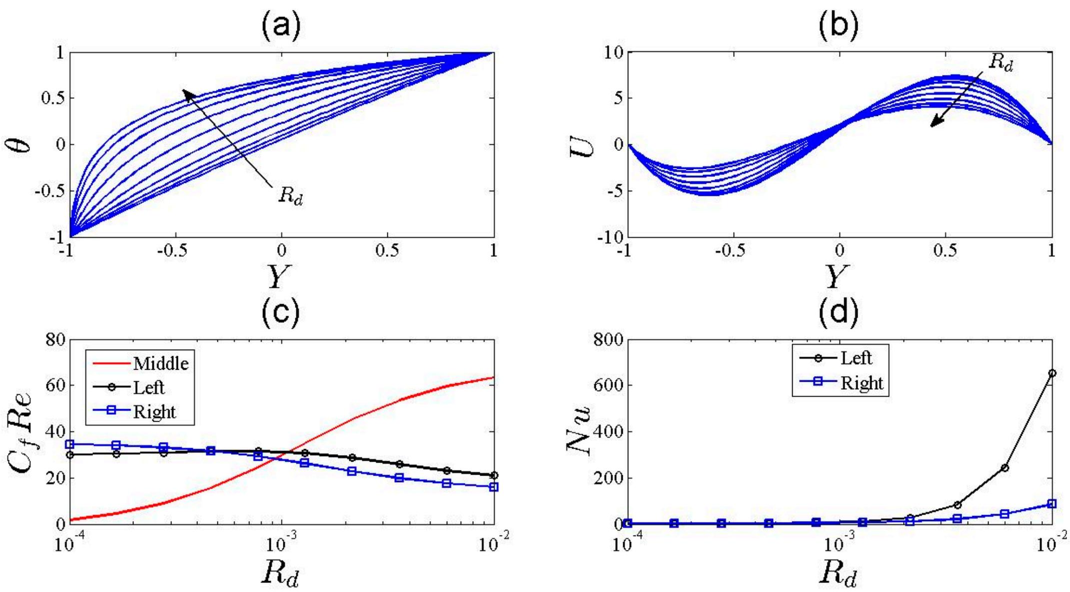

Figure 3. Thermal radiation effect on (**a**) the dimensionless temperature profile; (**b**) the dimensionless velocity profile; (**c**) the friction factor at walls and pressure gradient (middle); (**d**) Nusselt number at walls.

The effect of combined heat transfer coefficient (*Gr/Re*) is revealed in Figure 4. As exposed in Figure 4a with an increase of *Gr/Re* from 1 to 30 the dimensionless temperature is constant. Figure 4b illustrates the influence of the mixed convection parameter *Gr/Re*, on the dimensionless velocity profiles for the $R_d = 10$, and $\lambda_T = 0.01$, $\lambda_v = 0.01$, $We = 0.001$, $\theta_R = 10$, $Da = 0.1$. As seen the parabola shape function changes to a sine-like shape for the velocity profile. It seems that the sine-like shape for the velocity profile is an odd function but the absolute value of the right side is slightly higher than the left side.

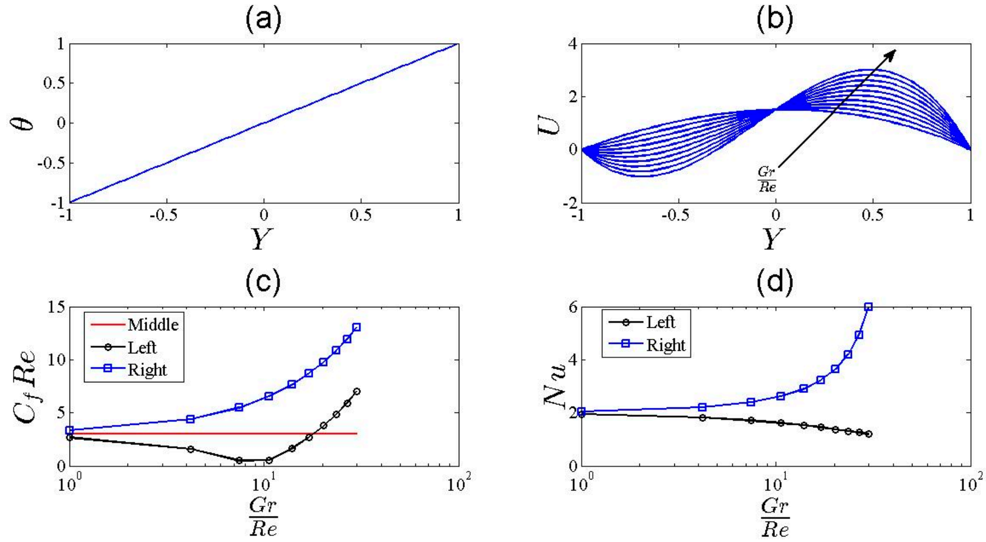

Figure 4. Grashof number to Reynolds number ratio effect on (**a**) the dimensionless temperature profile; (**b**) the dimensionless velocity profile; (**c**) the friction factor at walls and pressure gradient; (**d**) Nusselt number at walls.

In natural convection and heat transfer, the Grashof number (Gr) arises as a dimensionless number which approximates the ratio of the buoyancy to viscous force acting on a fluid. Notwithstanding, in forced convection the Reynolds number governs the fluid flow since in the current mixed convection problem the *Gr/Re* ratio is an important dimensionless parameter that governs the fluid flow. By increasing *Gr/Re*, the dimensionless velocity profile maximum increases and the location of the maximum moves from the middle to the right. It is obvious that the velocity is enhanced with increased buoyancy force. An increase of the reversal flow with the surge of *Gr/Re* and that the reversal flow is absent for small values of *Gr/Re*. The effect of *Gr/Re* on the friction factor at the walls and pressure gradient is illustrated in Figure 4c. For high *Gr/Re*, by increasing *Gr/Re*, the friction factors at the left and right walls are increased while the friction factor at the left is decreased for low *Gr/Re* values. Also the friction factor for the same Reynolds number is greater at the right wall rather than the left wall. As obvious from this figure, the natural convection augments the fluid flow near the hot wall and increases the wall skin fraction and diminishes the heat transfer near the cold wall and decreases it. The pressure gradient is constant and independent of *Gr/Re*. The same trend seen in Nusselt number at walls in Figure 4d, and that augmentation is more sensitive at the right wall.

The influence of Da is revealed in Figure 5. As exposed in Figure 5a by change of Darcy number from 0 to 15 for the $\lambda_T = 0.01$, $We = 0.001$, $\theta_R = 10$, $\lambda_v = 0.01$, $R_d = 10$, and $Gr/Re = 50$, the dimensionless temperature profile is not altered. Figure 5b displays the alteration of the sine-like contour of the velocity profile caused by the existence of the porous media. By increasing the Darcy number, the dimensionless velocity profile conserves its sine shape but its peaks are chamfered and its maximum decreases. As a result the general effect of the Darcy parameter is to decrease the velocity magnitude which is done by the solid matrix. This is as a result of the existence of the porous matrix which generates a resistive force akin to the drag force that acts in the opposite direction of the fluid motion, thus bringing the velocity of the fluid to decrease.

The effect of Darcy number on the friction factor at the walls and pressure gradient is exemplified in Figure 5c. By increasing of Darcy number, the friction factors at both walls are decreased for low Darcy number and increased for high Darcy number. The change of pressure gradients by Darcy number is significant. Physically, it means that with the increasing Ha, the strength of the solid matrix resistance, the resistance force increases which drags the flow backward and resists the effect of natural convection. It is observed that *dp/dx* increases rapidly with *Da*. The Darcy number effect on Nusselt number at the walls is shown in Figure 5d. Although the friction factor for the same Darcy number is greater at the right wall rather than the left wall, by increasing the Darcy number the Nusselt number decreases at the right wall and the Nusselt number increases at the left wall where both values approach to the same value.

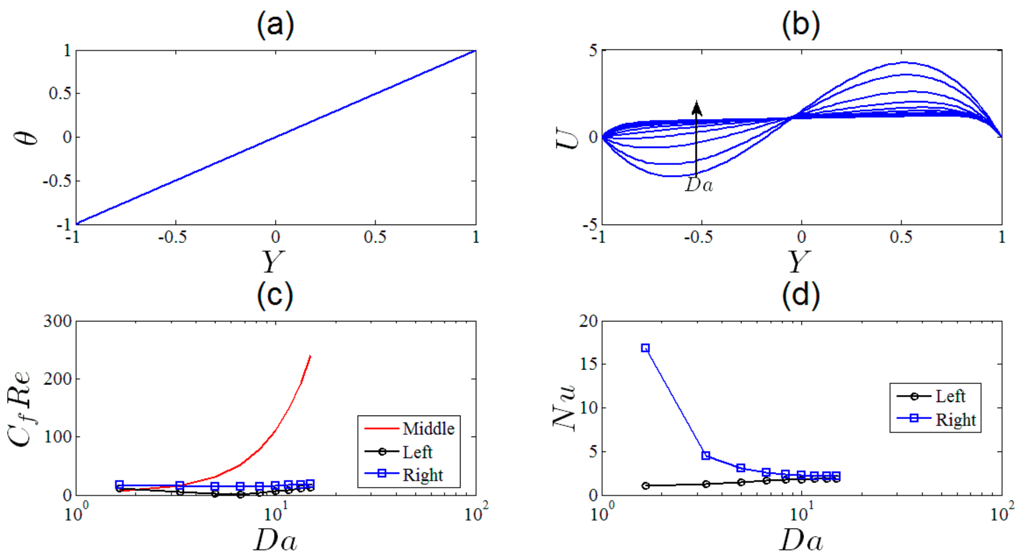

Figure 5. Darcy number effect on (**a**) the dimensionless temperature profile; (**b**) the velocity distribution; (**c**) the friction factor at walls and pressure gradient; (**d**) Nusselt number at walls.

The consequence of changing thermal parameter on the system is recognized in Figure 6. As shown in Figure 6a by increasing θ_R from 0.1 to 5 the dimensionless temperature is increased, especially near the left wall. The maximum value occurs at the right wall and the minimum value comes about at the left wall. Figure 6b shows the sine-like shape of the velocity profile for the $R_d = 0.01$, $Gr/Re = 100$, $We = 0.001$, $\lambda_T = 0.01$, $\lambda_v = 0.01$, and $Da = 0.1$. As observed, as θ_R increases, the dimensionless velocity profile conserves its sine-shape but displays its maximum decrease. As understandable from this figure the natural convection effects are weakened by the increase of θ_R. Furthermore, from Figures 3b and 6b it is detected that the increase of both radiation and thermal parameters make the reversal flow smaller, thus one consequence of radiation is the stabilization of the fluid motion as can be understood. The effect of θ_R on the pressure gradient and friction factor at walls is illustrated in Figure 6c. By increasing θ_R, the friction factor at the right wall is decreased slightly while the friction factor at the left wall is increased for $\theta_R < 3$ and decreased for $\theta_R > 3$. Also the friction factor for the $\theta_R < 2.5$ is greater at the wall $Y = 1$ while the friction factor at the wall $Y = -1$ is greater for the $\theta_R > 2.5$. In addition a slight pressure gradient decrease (the profile with the middle legend) is seen for $\theta_R < 0.5$, but a dramatic increase is detected for $\theta_R > 0.5$. The increase of θ_R has a slight effect on the walls' surface tension but it increases the *dp/dx* dramatically. Dimensionless temperature profiles are presented in Figures 3a, 4a, 5a and 6a disclose that the first derivative of the temperature profiles increases with the increase of the parameters θ_R and R_d while it decreases with an increase of *Gr/Re*. Therefore an increase in Nusselt number is seen by the increase in θ_R and R_d, while the augmentation of the Nusselt number is more at the right wall for $\theta_R < 3.5$ (see Figure 5d).

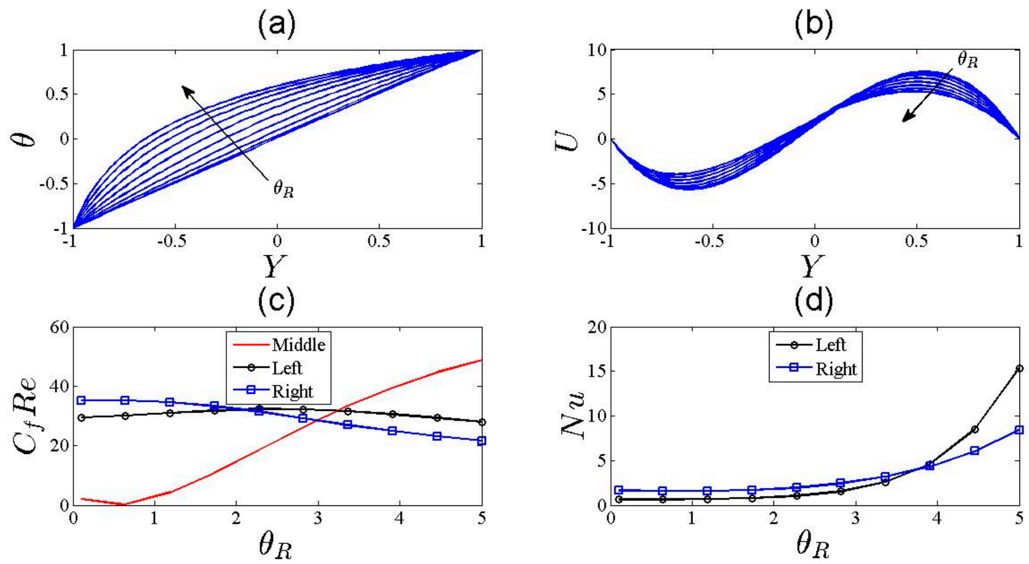

Figure 6. Thermal parameter effect on (**a**) the dimensionless temperature profile; (**b**) the dimensionless velocity distribution; (**c**) the friction factor at walls and pressure gradient; (**d**) Nusselt number at walls.

The outcome of velocity slip in the vertical microchannel velocity and temperature is presented in Figure 7 by changing velocity slip length from 0 to 0.05 for the R_d = 0.01, and λ_T = 0.01, θ_R = 0.1, *We* = 0.001, *Da* = 0.1, *Gr/Re* = 50. It can be seen from Figure 7a that for different values of the velocity slip length the dimensionless temperature is not changed. Further, in Figure 7b it is observed that amount of velocity increases at the right wall and decreases at the left wall with an increase of velocity slip, while the sinus shape of the velocity profile is not altered. The maximum value occurs at the right peak and it moves right by increase of the velocity slip. By increase of velocity slip length, the maximum dimensionless velocity profiles to some extent increase. The consequence of velocity slip length on the friction factor at walls and pressure gradient is illustrated in Figure 7c. It is clearly seen from these figures that *dp/dx* and the C_f at the Y = 1 increases while the C_f at the $Y = -1$ decrease with increasing velocity slip length. Also the friction factor for the same velocity slip length is greater at the right wall rather than the left wall. In Figure 7d, one can observe that the Nu at the $Y = -1$ is not changed considerably with an increase of velocity slip length, but the Nu at the Y = 1 increases rapidly, especially for $\lambda_v > 0.03$. The above discussion for the gas flow can be regarded by replacement of the velocity slip length by the mean free path of the molecules in a rare gas or velocity slip length by Knudsen number. By an upsurge of the gas viscosity and decrease of the gas density and the sound velocity in it, the velocity slip length increases.

The upshot of temperature slip is verified in Figure 8. As depicted in Figure 8a by increasing λ_T from 0 to 0.1 the magnitude of the dimensionless temperature distribution shifted upward with a constant value. This shows that the fluid temperature between the boundaries increases with increasing temperature slip length. Figure 8b illustrates the sine-like outline of the velocity side view with fixed values of other parameters as the R_d = 0.01, and *Gr/Re* = 50, *We* = 0.001, λ_v = 0.01, *Da* = 0.1, θ_R = 0.1. With increasing temperature slip, the dimensionless velocity profile is not changed much. Even though by increasing the temperature, the maximum velocity of the fluid increases, this increase are less than the increase in temperature for common values of the temperature slip. For the rare gas stream between parallel plates the temperature slip is proportional to the velocity slip length ratio or Knudsen number. By growth of the gas Prantdl number and decrease of the specific heat ratio, the temperature's slip length increases. The effect of temperature slip length on the friction factor at boundary conditions and pressure gradient is exemplified in Figure 8c. By increasing the temperature slip, the coefficient of friction at the walls is not changed meaningfully but the pressure gradient decreases slightly. The decrease of the pressure gradient in the gas can be justified by considering the definition of Prandtl number as the ratio of the viscous to the thermal diffusion. As a consequence, the fluid flow is resisted because of this predominant property of the viscous fluid that leads to the decrease in pressure gradient, so the temperature jumps the boundary condition because of the decrease in the required pumping power in comparison with no-jumps boundary condition. Furthermore the friction factor for the same temperature slip length is greater at the right wall than the left wall. The same trend is seen for the Nusselt numbers at walls as shown in Figure 8d.

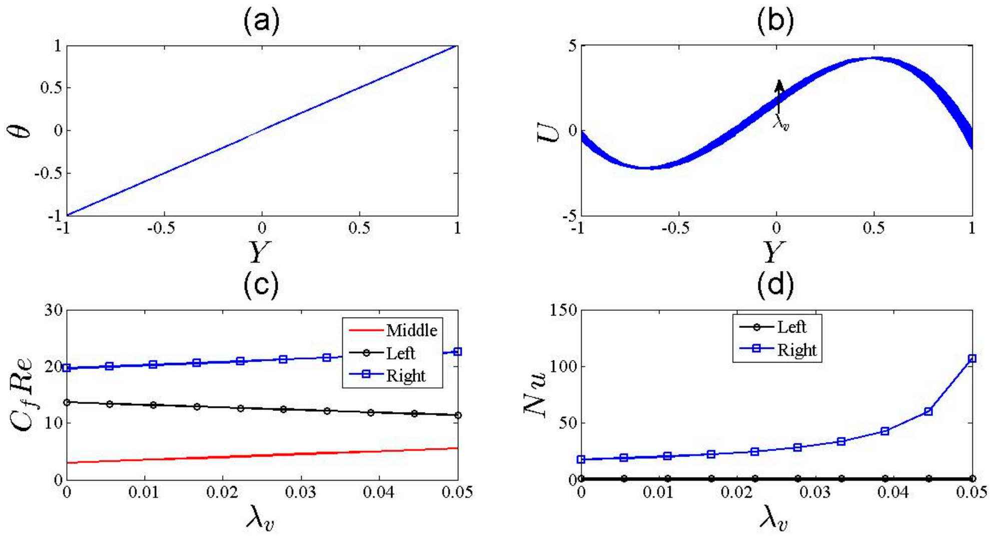

Figure 7. Velocity slip effect on (**a**) the dimensionless temperature distribution; (**b**) the dimensionless velocity profile; (**c**) the friction factor at walls and pressure gradient; (**d**) Nusselt number at walls.

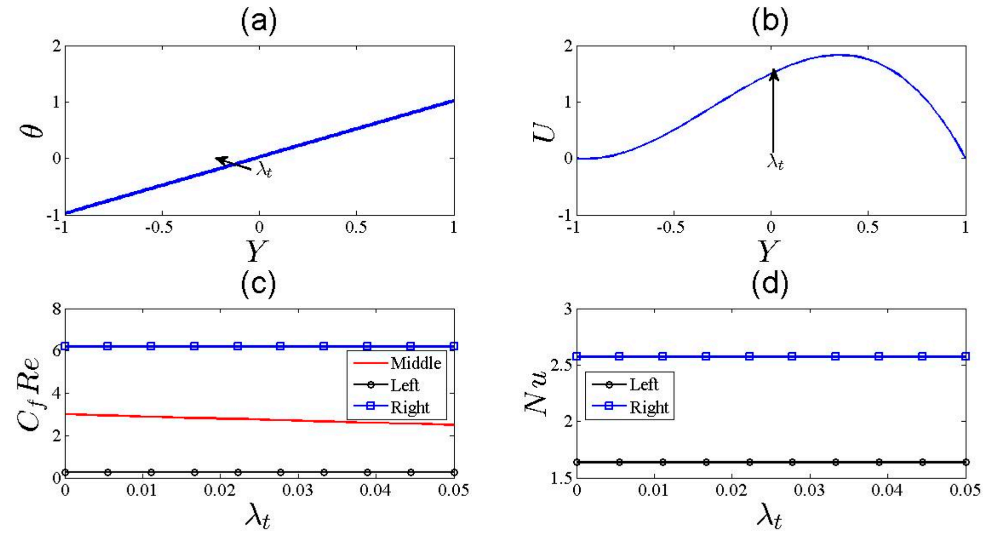

Figure 8. Temperature slip effect on (**a**) the dimensionless temperature distribution; (**b**) the dimensionless velocity profile; (**c**) the friction factor at walls and pressure gradient; (**d**) Nusselt number at walls.

The irreversibility in the channel flow of a fluid has two components of energy and momentum. Consequently, entropy production may occur as a result of fluid friction and heat transfer in the direction of finite temperature gradients. Following, Bejan [39,40], the volumetric rate of entropy generation can be expressed as:

$$\dot{S}_g''' = \frac{k}{T^2}\left(\frac{\partial T}{\partial y}\right)^2 + \frac{\mu}{T}\left(\frac{\partial u}{\partial y}\right)^2 \tag{30}$$

The first term in Equation (7) describes the heat transfer irreversibility and the second term represents the local entropy generation rate due to fluid friction, respectively. Figure 8 presents the effect of Darcy number on the dimensionless heat transfer component of the entropy, the dimensionless viscous component of the entropy, the total dimensionless heat transfer component of the entropy, and the total dimensionless viscous component of the entropy. The effect of Hartmann number is established in Figure 8. As shown in Figure 9a by the increase of Da from 16 to 18 for the R_d = 10, λ_T = 0.1, λ_v = 0.001, We = 0.001, θ_R = 5, and Gr/Re = 1, because the dimensionless temperature shape is not hooked on Darcy number the S_θ not altered. This narrow range of Darcy number is to emphasize the maximum exergy of a system. As exposed the $S_\theta(Y)$ is roughly linear and has a greater value at the left wall and a lesser value at the right wall. Figure 9b displays the distribution of S_u by the variation of compactness of the porous medium. The reality of compression of porous media produces a resistive force similar to the drag force that acts in the opposite direction of the fluid motion, thus causing the velocity of the fluid to decrease. By increasing of Darcy number, the peaks of the dimensionless velocity profile are chamfered consequently the velocity gradient inside the channel is decreased which leads to lesser viscous warming, so the overall effect of the Darcy number is to decrease the velocity component of entropy generation and it has an optimum near Da = 17.5.

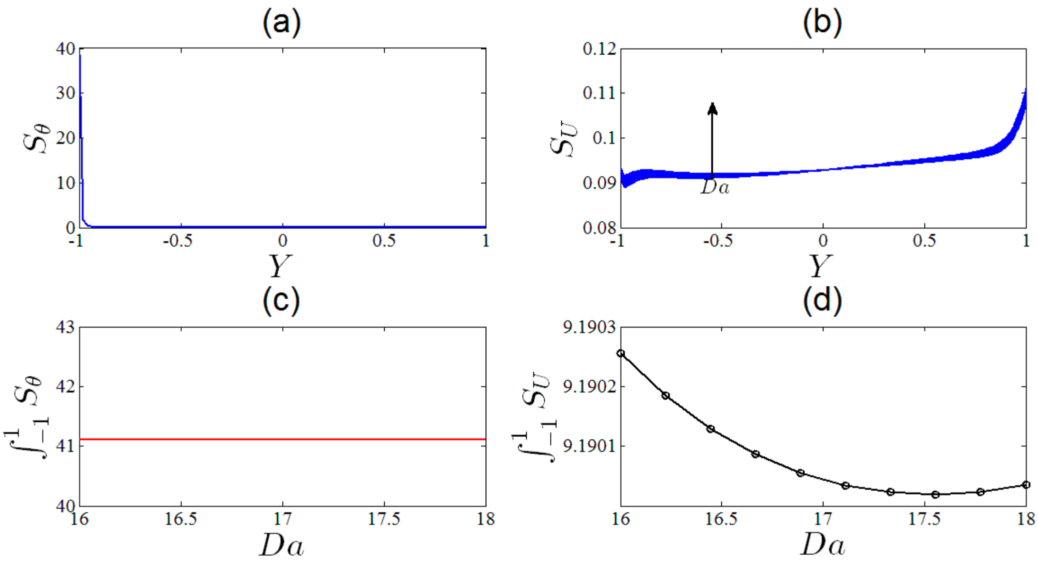

Figure 9. Darcy number effect on (**a**) the dimensionless heat transfer component of the entropy; (**b**) the dimensionless viscous component of the entropy; (**c**) the total dimensionless heat transfer component of the entropy; (**d**) the total dimensionless viscous component of the entropy.

4. Conclusions

The aim of this wprk was to describe the flow of a fully developed non-linear laminar mixed heat transfer of convection and radiation of an incompressible, electrically conducting radiative absorbing fluid in a vertical microchannel in the presence of a porous medium and the effects of thermal radiation heat absorption, and mixed convection. The consequences can be briefly summarized as follows:

(1) Temperature increases with increasing R_d and θ_R. As the radiation parameter increases the capacity of absorption of thermal radiation increases which causes higher temperatures. As well

the higher temperature parameter means a higher level of temperature of the system and an increase of radiation heat emitting sources.

(2) The heat transfer between the two boundaries of the channel is not simply due to pure conduction and the thermal radiation and mixed convection in a channel filled with a fluid-saturated porous medium has a great impact on heat exchange mechanisms.
(3) Dimensionless coefficients suitable for the evaluation of the dimensionless mean velocity, of the dimensionless bulk temperature and of the Nusselt numbers have been presented.
(4) Natural convection helps the fluid flow. As well the increase of temperature through the channel helps natural convection. However the existence of a porous solid matrix increases the pressure loss inside the channel. Since the pressure gradient decreases with increasing *Gr/Re*; R_d and θ_R while it increases with an increase of *Da*.
(5) The coefficient of skin friction increases as R_d and θ_R increase while it decreases with an increase of *Gr/Re*. The skin friction coefficient and mass transfer rates decrease with an increase in $\mathrm{R_d}$ whereas heat transfer rate increases with an increase in the parameter R_d.
(6) Coefficient of skin friction and Nusselt number increase with an increase of R_d and θ_R while they decrease with the mixed convection parameter.
(7) Grashof number, velocity slip, and pressure gradient increase skin friction and the Nusselt number, whereas temperature jump and Reynolds number reduce their values.
(8) The shape of velocity profiles is different when *Gr/Re* changes. By increasing *Gr/Re* it alternates from a parabola to a sine shape profile.
(9) The wall friction and Nusselt numbers may vary monotonically or non-monotonically with R_d and θ_R, again depending on the values of the other parameters.

Author Contributions: Mohamad Yaghoub Abdollahzadeh Jamalabadi designed the research with theoretical formulations. Payam Hooshmand performed the numerical simulations. Navid Bagheri and HamidReza KhakRah together analyzed the data and wrote the manuscript for initial submission. Majid Dousti had critical contribution in revising the manuscript including the preparation of responses and English correction. All authors have read and approved the final manuscript.

Conflicts of Interest: The authors declare no conflict of interest.

Nomenclature

Symbol	Description	Unit
C_p	specific heat capacity	J/(kg· K)
Da	Darcy number = $\frac{L^2}{K}$	
g	acceleration due to gravity	m/s^2
Gr	Grashof number = $\frac{g\beta(T_R-T_L)L^3}{2\nu^2}$	
h	heat transfer coefficient	$W/(m^2\cdot K)$
k	thermal conductivity	W/(m· K)
K	permeability of solid matrix	m^2
l	slip length	m
L	half of gap length	m
Nu	Nusselt Number = 2 Lh/k	
p	pressure	Pa
P	dimensionless pressure = $\frac{pL}{\mu\, u_m}$	
Pr	Prandtl number = υ/α	
R_d	the radiation parameter	
Re	Reynolds number = $\frac{u_m L}{\nu}$	

Symbol	Description	Unit
S	entropy	J/K
T	temperature	K
T_{ref}	reference temperature = $(\mathrm{T_L} + \mathrm{T_R})/2$	K
u	fluid vertical velocity	m/s
U	dimensionless fluid vertical velocit $y = u/u_\mathrm{m}$	
We	Weissenberg number = $\frac{\Gamma u_m}{L}$	
x, y	Cartesian coordinates	m
X, Y	dimensionless Cartesian coordinates = x/L; y/L	
Greek symbols		
α	thermal diffusivity	$\mathrm{m^2/s}$
β	volumetric coefficient of thermal expansion	1/K
χ	mean absorption coefficient of the medium	$\mathrm{m^{-1}}$
σ	Stefan–Boltzmann constant	$\mathrm{W/(m^2 \cdot K^4)}$
μ	dynamic viscosity	$\mathrm{kg/(m \cdot s)}$
υ	kinematic viscosity	$\mathrm{m^2/s}$
ρ	fluid density	$\mathrm{kg/m^3}$
Γ	stress relaxation time of the fluid	s
θ	dimensionless temperature = $\frac{2T-T_L-T_R}{T_R-T_L}$	
θ_R	temperature parameter	
Superscript		
0	reference	
L	Left wall	
m	average	
max	maximum	
min	minimum	
R	Right wall	
t	temperature	
v	velocity	

References

1. Tao, L.N. On Combined Free and Forced Convection in Channels. *J. Heat Transf.* **1960**, *82*, 233–238. [CrossRef]
2. Beckett, P.M. Combined Natural- and Forced-Convection between Parallel Vertical Walls. *SIAM J. Appl. Math.* **1980**, *39*, 372–384. [CrossRef]
3. Aung, W.; Worku, G. Theory of Fully Developed, Combined Convection Including Flow Reversal. *J. Heat Transf.* **1986**, *108*, 485–488. [CrossRef]
4. Lavine, A.S. Analysis of Fully Developed Opposing Mixed Convection between Inclined Parallel Plates. *Heat Mass Transf.* **1988**, *23*, 249–257. [CrossRef]
5. Cheng, C.H.; Kou, H.S.; Huang, W.H. Flow Reversal and Heat Transfer of Fully Developed Mixed Convection in Vertical Channels. *J. Thermophys. Heat Transf.* **1990**, *4*, 375–383. [CrossRef]
6. Hamadah, T.T.; Wirtz, R.A. Analysis of Laminar Fully Developed Mixed Convection in a Vertical Channel with Opposing Buoyancy. *J. Heat Transf.* **1991**, *113*, 507–510. [CrossRef]
7. Chauhan, D.S.; Kumar, V. Radiation effects on mixed convection flow and viscous heating in a vertical channel partially filled with a porous medium. *Tamkang J. Sci. Eng.* **2011**, *14*, 97–106.
8. Abdollahzadeh Jamalabadi, M.Y. Effects of Micro and Macro Scale Viscous Dissipations with Heat Generation and Local Thermal Non-Equilibrium on Thermal Developing Forced Convection in Saturated Porous Media. *J. Porous Media* **2015**, *18*, 843–860. [CrossRef]
9. Liu, D.; Garimella, S.V. Investigation of liquid flow in microchannels. *AIAA J. Thermo. Phys. Heat Transf.* **2004**, *18*, 65–72. [CrossRef]

10. Makhmalbaf, M.H.M. Experimental study on convective heat transfer coefficient around a vertical hexagonal rod bundle. *Heat Mass Transf.* **2012**, *48*, 1023–1029. [CrossRef]
11. Makhmalbaf, M.; Liu, T.; Merati, P. Experimental Simulation of Buoyancy-Driven Vortical Flow in Jupiter Great Red Spot. In Proceedings of the 68th Annual Meeting of the APS Division of Fluid Dynamics, Boston, MA, USA, 22–24 November 2015.
12. Forman, J.L.; Joodaki, H.; Forghani, A.; Riley, P.; Bollapragada, V.; Lessley, D.; Overby, B.; Heltzel, S.; Crandall, J. Biofidelity Corridors for Whole-Body Pedestrian Impact with a Generic Buck. *IRCOBI Conf.* **2015**, *49*, 356–372.
13. Abdollahzadeh Jamalabadi, M.Y. Effect of fuel inject angle on non-premixed combustion of air/methane mixturesin in vertical cylinder. *Int. J. Multidiscip. Res. Dev.* **2015**, *1*, 1–4.
14. Kandlikar, S.G.; Schmit, D.; Carrano, A.L.; Taylor, J.B. Characterization of surface roughness effects on pressure drop in microchannels. *Phys. Fluids* **2005**, *10*, 100606. [CrossRef]
15. Umavathia, J.C.; Sheremet, M.A. Mixed convection flow of an electrically conducting fluid in a vertical channel using Robin boundary conditions with heat source/sink. *Eur. J. Mech. B/Fluids* **2016**, *55*, 132–145. [CrossRef]
16. Zehra, I.; Yousaf, M.M.; Nadeem, S. Numerical Solutions of Williamson Fluid with Pressure Dependent Viscosity. *Results Phys.* **2015**, *5*, 20–25. [CrossRef]
17. Singh, K.D. MHD mixed convection visco-elastic slip flow through a porous medium in a vertical porous channel with thermal radiation. *Kragujev. J. Sci.* **2013**, *35*, 27–40.
18. Abdollahzadeh Jamalabadi, M.Y.; Park, J.H. Thermal radiation, joule heating, and viscous dissipation effects on mhd forced convection flow with uniform surface temperature. *Open J. Fluid Dyn.* **2014**, *2*, 125–132. [CrossRef]
19. Abdollahzadeh Jamalabadi, M.Y. Analytical Study of Magnetohydrodynamic Propulsion Stability. *J. Mar. Sci. Appl.* **2014**, *3*, 281–290. [CrossRef]
20. Shahidian, A.; Ghassemi, M.; Khorasanizade, S.; Abdollahzade, M.; Ahmadi, G. Flow Analysis of Non-Newtonian Blood in a Magnetohydrodynamic Pump. *IEEE Trans. Magn.* **2009**, *6*, 2667–2670. [CrossRef]
21. Takagi, D.; Huppert, H.E. Viscous gravity currents inside confining channels and fractures. *Phys. Fluids* **2008**, *20*. [CrossRef]
22. Longo, S.; di Federico, V.; Chiapponi, L. Propagation of viscous gravity currents inside confining boundaries: The effects of fluid rheology and channel geometry. *Proc. R. Soc. Lond. A Math. Phys. Eng. Sci.* **2015**, *471*. [CrossRef]
23. Gerami, A.; Allaire, P.; Fittro, R. Control of Magnetic Bearing with Material Saturation Nonlinearity. *J. Dyn. Syst. Meas. Control* **2015**, *137*, 061002. [CrossRef]
24. Gerami, A.; Allaire, P.; Fittro, R. Nonlinear Modeling and Control of a Magnetic Bearing with Material Saturation. In Proceedings of the 14th International Conference on Magnetic Bearings, Linz, Austria, 11–14 August 2014.
25. Dousti, S.; Dimond, T.W.; Allaire, P.E.; Wood, H.E. Time Transient Analysis of Horizontal Rigid Rotor Supported with O-Ring Sealed Squeeze Film Damper. In Proceedings of the ASME 2013 International Mechanical Engineering Congress and Exposition, San Diego, CA, USA, 15–21 November 2013.
26. Dousti, S.; Gerami, A.; Dousti, M. A Numerical CFD Analysis on Supply Groove Effects in High Pressure, Open End Squeeze Film Dampers. *Int. J. Eng. Innov. Res.* **2016**, *1*, 80–89.
27. Asfer, M.; Panigrahi, P.K. Boundary Slip of Liquids. In *Encyclopedia of Microfluidics and Nanofluidics*; Springer-Verlag US: New York, NY, USA, 2015; pp. 193–202.
28. Karniadakis, G.; Beskok, A.; Aluru, N. Governing Equations and Slip Models, Microflows and Nanoflows. *Fundam. Simul.* **2005**, *29*, 51–77.
29. Ulmanella, U.; Ho, C.M. Molecular effects on boundary condition in micro/nanoliquid flows. *Phys. Fluids* **2008**, *20*, 1–9. [CrossRef] [PubMed]
30. Bocquet, L.; Barrat, J.-L. Flow Boundary Conditions from Nano- to Micro-Scales. *Soft Matter* **2007**, *3*, 685–693. [CrossRef]
31. Karniadakis, G.; Beskok, A.; Aluru, N. *Microflows and Nanoflows: Fundamentals and Simulation*; Springer: New York, NY, USA, 2005.
32. Jha, B.K.; Aina, B.; Isa, S. Fully developed MHD natural convection flow in a vertical annular microchannel: An exact solution. *J. King Saud Univ. Sci.* **2015**, *27*, 253–259. [CrossRef]

33. Williamson, R.V. The Flow of Pseudoplastic Materials. *Ind. Eng. Chem.* **1929**, *21*, 1108–1111. [CrossRef]
34. Longo, S.; di Federico, V.; Chiapponi, L. Non-Newtonian Power-Law Gravity Currents Propagating in Confining Boundaries. *Environ. Fluid Mech.* **2015**, *15*, 515–535. [CrossRef]
35. Takagi, D.; Huppert, H.E. Initial advance of long lava flows in open channels. *J. Volcanol. Geotherm. Res.* **2010**, *195*, 121–126. [CrossRef]
36. King, S.E.; Woods, A.W. Dipole solutions for viscous gravity currents: Theory and experiments. *J. Fluid Mech.* **2003**, *483*, 91–109. [CrossRef]
37. Longo, S.; di Federico, V.; Chiapponi, L. A dipole solution for power-law gravity currents in porous formations. *J. Fluid Mech.* **2015**, *778*, 534–551. [CrossRef]
38. Zheng, Z.; Soh, B.; Huppert, H.E.; Stone, H.A. Fluid drainage from the edge of a porous reservoir. *J. Fluid Mech.* **2013**, *718*, 558–568. [CrossRef]
39. Bejan, A. Second-law analysis in heat transfer and thermal design. *Adv. Heat Transf.* **1982**, *15*, 1–58. [CrossRef]
40. Bejan, A. *Entropy Generation Minimization*; CRC: Boca Raton, FL, USA, 1996.

© 2016 by the authors; licensee MDPI, Basel, Switzerland. This article is an open access article distributed under the terms and conditions of the Creative Commons Attribution (CC-BY) license (http://creativecommons.org/licenses/by/4.0/).